RESEARCH PAPER

PCCP
www.rsc.org/pccp

Theoretical evidence for the formation of rotational energy level clusters in the vibrational ground state of PH_3

Sergei N. Yurchenko,[a] Walter Thiel,[a] Serguei Patchkovskii[b] and Per Jensen*[c]

[a] *Max-Planck-Institut für Kohlenforschung, Kaiser-Wilhelm-Platz 1, D-45470 Mülheim an der Ruhr, Germany*
[b] *Steacie Institute for Molecular Sciences, National Research Council of Canada, Ottawa, Ontario, Canada K1A 0R6*
[c] *FB C-Theoretische Chemie, Bergische Universität, D-42097 Wuppertal, Germany. E-mail: jensen@uni-wuppertal.de; Fax: +49 202 439 2509; Tel: +49 202 439 2468*

Received 30th November 2004, Accepted 11th January 2005
First published as an Advance Article on the web 28th January 2005

We investigate theoretically the rotational dynamics of pyramidal XY_3 molecules in highly excited rotational states. Towards this end we compute, by a variational method, the rotational energy levels in the vibrational ground state of PH_3 for $J \leq 80$. At $J \geq 50$ the calculated energy levels show a distinct cluster pattern. By monitoring the cluster formation we follow the various stages of the rotational dynamics. We analyze the wavefunctions for the cluster states and compute expectation values which show that the C_{3v} geometrical symmetry of PH_3 is broken at high rotational excitation. The conclusions drawn from the quantum-mechanical calculations are confirmed by semi-classical theory, *i.e.*, by an analysis of the stationary points on the rotational energy surface.

I. Introduction

Advances in experimental techniques for laser alignment and manipulation of molecules have made it possible to study 'orientation' effects in chemical reactions, spectroscopy, and photodissociation (For review see ref. 1). Thus, molecules can be prepared in given $|J,k,m\rangle$ rotational states (for example with the electrostatic hexapole technique[2]) or they can be spun to acquire very high angular momenta.[3] Fast rotation can cause dissociation[4] or it can stabilize the molecular rotation about a specific molecule-fixed axis.[5,6] Furthermore, rotational energy can modify the molecular potential energy surface,[3] and bring about qualitative changes of the spectral pattern, such as energy cluster formation[5–7] or monodromy effects.[8–10] The development of methods for aligning molecules generally requires detailed knowledge of the rotational dynamics, including rovibrational wavefunctions at high rotational excitation.[1] Such knowledge must also be available for field-free molecules since in many aligning applications, it is necessary that the molecules eventually be free of the field that induces their spatial orientation.

Many symmetrical hydrides XH_N ($N = 2, 3, 4$) with heavy central nuclei X exhibit so-called local mode effects.[11–13] One property of these molecules, of direct interest here, is that their bond angles are close to 90°; see Table 1 of ref. 12. As a result, the stretching vibrations are naturally orthogonal, and the kinetic-energy intermode interactions are small, as are the interactions originating in the potential energy function. This behaviour becomes even more pronounced for highly excited vibrational states.[13,14] Furthermore, at high rotational excitation the rotational motion is also, in a sense, orthogonal to the stretching vibrational motion.[13] That is, the small Coriolis interaction does not destabilize the rotational motion. The rotational energy levels of the corresponding molecular states form well separated, near-degenerate energy clusters.[7,15–24] In the cluster states (or *localized states*), the molecule rotates about a so-called localization axis which is approximately parallel to one of the X–H bonds.[6,25,26] The existence of the cluster states was theoretically predicted for H_2O, H_2S, H_2Se, H_2Te, CH_4, CF_4, SiH_4, SbH_4 and SF_6 by semi-classical methods and quantum-mechanical, variational calculations of rotation–vibration energy levels.[5,6,13,14,25–34] Semi-classically, the cluster states are characterized by 'stationary points' on rotational energy surfaces.[6,21,35] A bifurcation analysis of the rotational energy surface determines the localization axes and predicts the critical angular momentum value J_c at which the cluster formation sets in.[6,25,36] The energy clusters have been experimentally observed for H_2Se,[30,37,38] CH_4, SiH_4 (see ref. 33 and references therein), and SF_6.[39]

Formation of energy clusters at high rotational excitation is a well-established phenomenon for XH_2 and XH_4 molecules. The energy cluster formation is intimately linked to local mode effects[13] and most XH_3 molecules, including PH_3, satisfy the 'structural local mode requirements' of Halonen and Robiette.[12] Thus, we expect energy cluster formation to take place also for XH_3 molecules, even though this has never been discussed extensively so far.

The present work is concerned with highly excited rotational states of PH_3 molecules in the absence of external fields. We calculate rotational term values in the vibrational ground state of PH_3 for $J \leq 80$ with a variational quantum-mechanical model. This model is outlined in Section II, where we also introduce the basis set and discuss the convergence of the calculations. The computed term values (which, as expected, exhibit cluster formation) are described in Section III. We compare them with the eigenvalues of a standard effective Hamiltonian involving rotational constants and centrifugal distortion constants. In Section IV we present wavefunction analysis for the cluster states. We determine the localization axes, calculate effective bond lengths and bond angles, and present probability density functions in terms of the Euler angles. With this information, we visualize the dynamics in highly excited rotational states of PH_3. Highly excited rotational states can often be adequately described by

DOI: 10.1039/b418073a

semi-classical models, so we report in Section V a semi-classical analysis of the cluster formation; this analysis is based on the theory of rotational energy surfaces (see, for example, ref. 6). We show that the semi-classical description yields results similar to those obtained by quantum mechanical methods, and this allows us to extend our study to states with $J > 80$. Finally in Section VI we offer conclusions and discuss the prospects of applying the results of this work to laser manipulation of molecular rotation.

II. Computational details

The rotation–vibrational Schrödinger equation is solved variationally, *i.e.*, by diagonalizing a matrix representation of the rovibrational Hamiltonian. The theoretical approach for calculating the rotation–vibration energies of an XY_3 molecule from the potential energy function has been described in refs. 40 and 41 and we refer the reader to these publications for details. Here we give only a few essential points required for understanding the wavefunction analysis.

The matrix representation of the rovibrational Hamiltonian is constructed in terms of the 'primitive' basis:

$$\phi_{v,k}^{J,m} = |J,k,m\rangle|v_{\rm inv}\rangle|v_1\rangle|v_2\rangle|v_3\rangle|v_4,l_4\rangle, \qquad (1)$$

where the $|J,k,m\rangle$ are standard rigid rotor rotational wavefunctions (see, for example, ref. 42), $|v_{\rm inv}\rangle$ describes the inversion motion, $|v_i\rangle$, $i = 1,2,3$, are 1D Morse oscillator functions, each describing a local stretching mode, and $|v_4,l_4\rangle$ are 2D isotropic harmonic oscillator functions describing bending motion other than the inversion. The $|v_{\rm inv}\rangle$ functions are obtained by numerical solution of 1D inversion Schrödinger equation with the Numerov–Cooley technique.[43–45] The wavefunction ($\phi_{v,k}^{J,m}$ is expressed in terms of the coordinates described in refs. 40 and 41. These coordinates are the inversion coordinate ρ, the rotational Euler angles θ, ϕ, χ,[42,46] linearized versions of the internuclear distances r_1, r_2, r_3, and linearized, non-redundant linear combinations of the bond angles $\alpha_1 = \angle(H_2PH_3)$, $\alpha_2 = \angle(H_1PH_3)$, and $\alpha_3 = \angle(H_1PH_2)$ (see Fig. 1). Following ref. 41 we denote the five linearized coordinates mentioned above as ξ_λ^l, $\lambda = 1, \ldots, 5$. When the molecule is in the *reference configuration*[41] with C_{3v} geometrical symmetry, ρ is the angle between the C_3 axis (which is the molecule-fixed z axis) and any one of the P–H bonds. In less symmetrical configurations, ρ is determined by the Eckart–Sayvetz conditions[41] and has no immediate geometrical interpretation. In eqn. (1) the index v is a shorthand notation for the vibrational quantum numbers ($v_{\rm inv}$, v_1, v_2, v_3, v_4 and l_4), k ($= -J, -J+1, \ldots, J$) is the projection of the total angular momentum onto the molecule-fixed z axis (which is the c axis[42] for PH_3), and m ($= -J, -J+1, \ldots, J$) is the projection of the total angular momentum on the space-fixed Z axis.[41]

In the variational calculations the expansions[41] of the kinetic energy factors $G_{\alpha\beta}$, the pseudo-potential U, and the potential energy V are taken to 4th order. In the numerical integration of the inversion Schrödinger equation a grid of 1000 points was used. The basis set is truncated so that

$$P = 2(v_1 + v_2 + v_3) + v_{\rm inv} + v_4 \leq 6 \qquad (2)$$

The limit $P \leq 6$ means that the $J = 80$ matrix blocks corresponding to A_1, A_2, and E symmetry in the molecular symmetry group $C_{3v}(M)$ [see eqn. (4) below] have the dimensions $N(A_1) = 6966$, $N(A_2) = 6931$ and $N(E) = 13901$, respectively. We use a rather small vibrational basis set here because at present, we are only concerned with the rotational term values in the vibrational ground state. Besides, we are not aiming at an extreme accuracy for the numerical results but rather at extracting qualitative information about the cluster phenomenon. The PH_3 potential energy surface is taken from ref. 47 where the *ab initio* potential energy surface from ref. 48 was refined in simultaneous fittings to *ab initio* data and to the available, experimentally determined vibrational term values of PH_3.

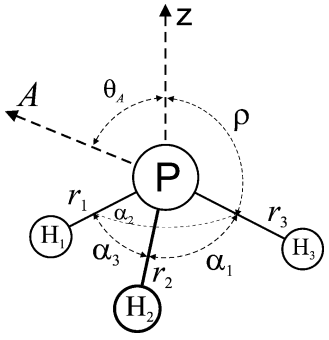

Fig. 1 The labeling of the nuclei chosen for PH_3, the relevant coordinates, the molecule-fixed z axis, and the localization axis A (see text).

III. Calculated rotational term values

The calculated rotational term value spacings $E_{Jk} - E_J^{\rm max}$ are shown in Fig. 2. Here, E_{Jk} is the energy of the level characterized by the quantum numbers J, k (see, for example, ref. 42) and $E_J^{\rm max}$ is the maximum energy in the J multiplet. For the oblate symmetric top PH_3 (see Section 11.2.1 of ref. 42), the highest energy $E_J^{\rm max}$ in the J multiplet corresponds to $k = 0$, whereas the states with $|k| = J$ have the lowest energies.

In the crude approximation of the PH_3 molecule being rigid, the term value spacings $E_{Jk} - E_J^{\rm max}$ are independent of J and given by the simple expression[42]

$$E_{Jk} - E_J^{\rm max} = (C_e - B_e)\, k^2. \qquad (3)$$

Here, $B_e > C_e$ are the rotational constants of the rigid PH_3 molecule.

As seen from Fig. 2, for low J (and, therefore, low k), the calculated energy spacings are indeed nearly independent of J and follow eqn. (3) closely. However, as J increases, centrifugal distortion causes the spacings between the highest energies in Fig. 2 to vary significantly with J in such a way that near-degenerate energy clusters are formed. This cluster formation is analogous to that in XH_2 molecules (see, for example, refs. 25, 26, 31, 49 and 50).

We label the wavefunctions of PH_3 in the molecular symmetry group[42]

$$C_{3v}(M) = \{E, (123), (132), (12)^*, (13)^*, (23)^*\} \qquad (4)$$

where E is the identity operation, (123) and (132) are cyclic permutations of the three protons (labeled 1, 2, 3) in PH_3 and each of the permutation-inversion operations (12)*, (13)* and (23)* involves interchange of two protons and inversion of all particles in the molecular center of mass.[42] The irreducible representations of $C_{3v}(M)$ are given in Table A-6 of ref. 42. For a given value of J, the highest four energy levels, taken in descending order, have $|k| = 0, 1, 2, 3$ in rigid rotor notation. The level with $|k| = 0$ gives rise to a single rovibronic wavefunction with A_1 symmetry in $C_{3v}(M)$ for J even and A_2 symmetry for J odd (see Section 12.4 of ref. 42). The levels with $|k| = 1$ and 2 each give rise to a doubly degenerate wavefunction pair of E symmetry, and the level with $|k| = 3$ corresponds to two rovibronic wavefunctions with symmetries A_1 and A_2, respectively. These two states are degenerate for the rigid molecule but, because of centrifugal distortion, they can split apart in the vibrating molecule.

Inspection of Fig. 2 shows that at $J > 50$ or so, an energy cluster (called the 'top cluster' here) is formed by the states with $|k| = 0, 1, 2$ together with *one* of the two states with $|k| = 3$. These two $|k| = 3$ states are near-degenerate for low J but

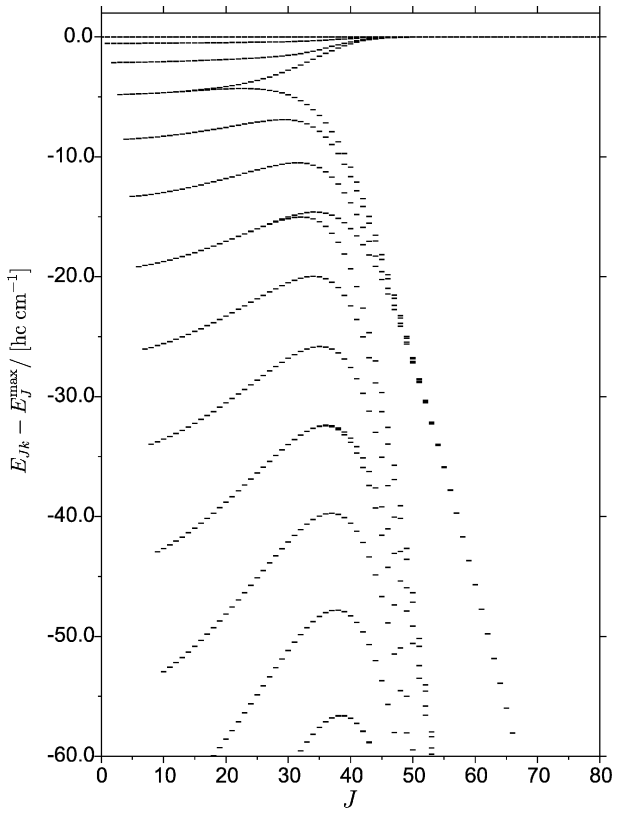

Fig. 2 The calculated rotational energy structure in the vibrational ground state of PH_3. Term values $E_{J,k}$ are plotted relative to the highest term E_J^{max} for each J multiplet. From top to bottom, successive curves correlate with rigid-rotor states having increasing values of $|k| = 0, 1, 2,....$

split rapidly apart for $J > 25$. We determine empirically that the symmetry of the $|k| = 3$ state in the top cluster is always such that the six cluster states span the C_{3v}(M) representation

$$\Gamma_{\text{cluster}} = A_1 + A_2 + 2\,E. \qquad (5)$$

That is, for even J, when the $k = 0$ state corresponds to A_1 symmetry, the top cluster contains the $|k| = 3$ state with A_2 symmetry, whereas for J odd, it contains the $|k| = 3$ state with A_1 symmetry. There are six clusters states in total, but two pairs of them have E symmetry in C_{3v}(M) and are each doubly degenerate. Consequently, the energy clusters in Fig. 2 are formed by coalescence of four distinct energy levels. As J increases, more clusters form below the top cluster.

It is important to ensure the adequacy of the vibrational basis used in the present calculations. The size of the vibrational basis set is controlled by the condition in eqn. (2). We have found that at $J = 40$, the truncation $P \leq 6$ provides convergence to within 0.5 cm^{-1} for the top cluster energies, and to within 0.001 cm^{-1} for the corresponding energy differences $E_{Jk} - E_J^{max}$ (Fig. 2). Similarly, at $J = 60$ the top energy level is converged to within $\approx$3 cm^{-1}. For this J value, the four energy levels in the top cluster coincide to within 10^{-4} cm^{-1} which indicates a comparable convergence of the energy differences.

By following the arguments given for XH_2 molecules in ref. 51 we explain why the cluster states have the symmetry Γ_{cluster} in eqn. (5). As already mentioned, we can describe the energy clusters in terms of localized states in which the molecule rotates about a localization axis approximately coinciding with one of the X–H bonds. We assume that we know one such localized state (or *primitive cluster state*, PCS), say $|1\ \text{PCS}\rangle$. In the state $|1\ \text{PCS}\rangle$, the molecule rotates about the X–H_1 bond in such a way that an observer on proton 1 would see the rest of the molecule rotate clockwise. Obviously, there exist another five localized states equivalent to $|1\ \text{PCS}\rangle$; we obtain these states by applying the symmetry operations in C_{3v}(M) to $|1\ \text{PCS}\rangle$: $|2\ \text{PCS}\rangle = (123)\ |1\ \text{PCS}\rangle$, $|3\ \text{PCS}\rangle = (132)\ |1\ \text{PCS}\rangle$, $|4\ \text{PCS}\rangle = (12)^*\ |1\ \text{PCS}\rangle$, $|5\ \text{PCS}\rangle = (13)^*\ |1\ \text{PCS}\rangle$ and $|6\ \text{PCS}) = (23)^*\ |1\ \text{PCS}\rangle$). In each of the six primitive cluster states $|j\ \text{PCS}\rangle$, $j = 1, 2, \ldots, 6$, the molecule rotates about one of the three bonds X–H_1, X–H_2 or X–H_3 in a clockwise or anticlockwise manner. It is straightforward to show by standard group theoretical methods[42] that the six corresponding wavefunctions span the reducible C_{3v}(M) representation Γ_{cluster} given in eqn. (5).

For a rigid PH_3 molecule, k is a good quantum number in that each energy level of the rigid symmetric rotor can be uniquely labeled by a k value. For the vibrating molecule described by our variational calculations, k is no longer a good quantum number since the rotation–vibration wavefunctions $\psi_n^{J,\Gamma}$ are linear combinations of basis functions $\phi_{v,k}^{J,m}$ [eqn. (1)] with different k values:

$$\psi_n^{J,\Gamma}(r_1, r_2, r_3, \alpha_1, \alpha_2, \alpha_3, \theta, \phi, \chi) = \sum_{k=-J}^{J} \sum_{v} C_{v,k}^{n,J,\Gamma} \phi_{v,k}^{J,m}, \qquad (6)$$

where the $C_{v,k}^{n,J,\Gamma}$ are expansion coefficients, Γ is the C_{3v}(M) symmetry of the wavefunction $\psi_n^{J,\Gamma}$, n is an index distinguishing eigenfunctions with the same value of Γ, and v is defined in connection with eqn. (1). We label the energies determined in the variational calculation by the k value k_{lc} (where the subscript letters 'lc' stand for 'largest contribution') of the basis function ($\phi_{v,k}^{J,m}$ with the largest contribution to the eigenfunction $\psi_n^{J,\Gamma}$, *i.e.*, with the largest value of $|C_{v,k}^{n,J,\Gamma}|^2$. For low J we find $k_{\text{lc}} = k$, where k is the angular momentum projection value expected from rigid-rotor theory. As J increases, contributions from the primitive basis functions in eqn. (1) are being redistributed. For example, at $J = 50$, the eigenfunctions of the states in the top cluster have dominant contributions from the basis functions with $K = |k| = 9, 11, 12, 13, 15, 16$:

$$\begin{aligned}
\psi_1^{A_1} &= [0.48 \times |12,+\rangle + 0.44 \times |9,+\rangle + 0.40 \times |15,+\rangle] \\
&\quad |v = 0\rangle + \ldots \\
\psi_{2,3}^{E} &= [0.34 \times |11,\pm\rangle + 0.33 \times |13,\pm\rangle - 0.25 \times |16,\pm\rangle] \\
&\quad |v = 0\rangle + \ldots \\
\psi_{4,5}^{E} &= [0.34 \times |11,\pm\rangle - 0.33 \times |13,\pm\rangle + 0.25 \times |16,\pm\rangle] \\
&\quad |v = 0\rangle + \ldots \\
\psi_6^{A_2} &= [0.48 \times |12,-\rangle - 0.44 \times |9,-\rangle + 0.40 \times |15,-\rangle] \\
&\quad |v = 0\rangle + \ldots \qquad (7)
\end{aligned}$$

where $|K, \pm\rangle$ is a symmetric (+) or antisymmetric (−) combination of rigid-rotor wave-functions $|J,k,m\rangle$ (see ref. 41) and $|v = 0\rangle$ stands for the product of the primitive vibrational basis functions correlating with the vibrational ground state wavefunction, *i.e.* $v_{\text{inv}} = v_1 = v_2 = v_3 = v_4 = l_4 = 0$ in eqn. (1). As in eqn. (7), we generally denote by ψ_i^{Γ}, $i = 1, 2, \ldots, 6$, the wavefunctions $\psi_n^{J,\Gamma}$ belonging to a particular top cluster (at a given J value), where Γ is the C_{3v}(M) symmetry of the wavefunction in question. The wavefunctions with $\Gamma = E$ and $i = 2, 3$ belong to the one degenerate E state, those with $\Gamma = E$ and $i = 4, 5$ belong to the other E state. The eigenvalues corresponding to the wavefunctions $\psi_1^{A_1}$, $\psi_{2,3}^{E}$, $\psi_{4,5}^{E}$ and $\psi_6^{A_2}$ in eqn. (7) are 10685.960, 10685.957, 10685.950 and 10685.946 cm^{-1}, respectively.

In Fig. 3 we compare the term values of Fig. 2 to rotational term values calculated from an effective rotational Hamiltonian[52] with the QWanew program.[53] We use experimentally determined spectroscopic parameters from ref. 54 that have been obtained by fitting to experimental transition wavenumbers involving states with $J \leq 23$; the resulting standard deviation was 4.39×10^{-7} cm^{-1}.[54] Our calculations are in good agreement with these 'experimentally derived' term values for $J \leq 35$. At higher J values we obtain smaller separations between the clusters. In our calculations, the energy separations between the clusters at high J vary linearly with

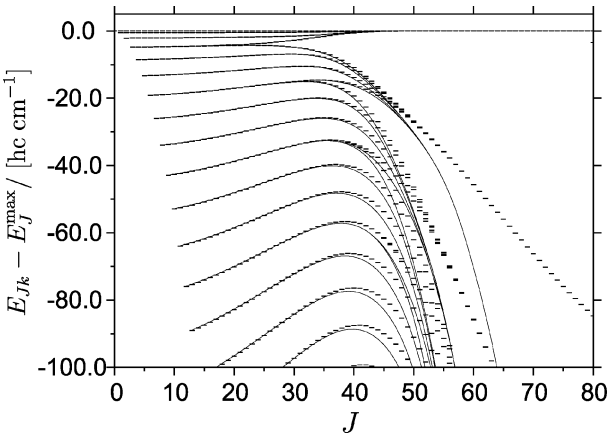

Fig. 3 Calculated rotational energy levels of PH_3 in the ground vibrational state plotted relative to the highest term for each J multiplet. Variationally calculated term values are drawn as short horizontal lines. Solid curves represent the eigenvalues of an effective rotational Hamiltonian with parameters obtained by fitting to experimental data.[54] From top to bottom, successive curves correlate with rigid-rotor states having increasing values of $|k| = 0, 1, 2, ...$

J; this is consistent with the expectation that in these states, the rotational energy varies essentially as $B_{loc}k_{loc}^2$ (B_{loc} is the rotational constant value associated with rotation about the localization axis and $k_{loc} = J, J-1, \ldots$ is the projection of the angular momentum on this axis in units of $\hbar$). The cluster spacings obtained from the effective Hamiltonian are not linear in J, which is an indication that the effective-Hamiltonian treatment is not converged for high rotational states.

An element of the semi-classical theory described in Section V below (see also ref. 6) is the critical J value J_c: When J passes through the J_c value, the molecular rotational motion undergoes critical changes and energy clusters start forming. It is not clear how to obtain J_c from our variational results in Fig. 2. One could perhaps say that the first significant deviation from the rigid-rotor energy pattern [eqn. (3)] occurs when the two levels with $|k| = 3$ split apart and the upper level starts approaching the $|k| = 0, 1, 2$ levels. This happens around $J = 15$. In the following sections we address this issue and try to quantify, by means of wavefunction analysis, the critical value of J.

IV. Wavefunction analysis

We now study the eigenfunctions obtained from the variational calculations in order to explain the nature of the rotational motion in the cluster states. In this context, we determine the rotational localization axes for the cluster states and analyze the changes in the molecular geometry of PH_3 resulting from centrifugal distortion.

We focus on the eigenfunctions ψ_i^Γ, $i = 1, 2, \ldots, 6$, of the top cluster, and we first aim at visualizing these wavefunctions. They depend on nine coordinates so it is not obvious how to plot them. We are primarily concerned with the rotational motion in the ground vibrational state. Therefore, we reduce the dimensionality by integrating the square of ψ_i^Γ over all vibrational coordinates, and over the Euler angle ϕ. This is an example of the reduction of density matrices treated, for example, by Feynman.[55] We obtain the rotational probability distribution:

$$F(\theta,\chi) = \int \mathrm{d}V \mathrm{d}\phi\ (\psi_i^\Gamma)^*\ \psi_i^\Gamma\ \sin\theta, \qquad (8)$$

where $\mathrm{d}V$ is the volume element associated with the vibrational coordinates. The wavefunction square $(\psi_i^\Gamma)^*\ \psi_i^\Gamma$ is independent of the Euler angle ϕ because the ϕ-dependence of each function ψ_i^Γ is expressed by the factor $\exp(im\phi)/\sqrt{2\pi}$.[56] Thus, the rotational probability density function F naturally depends only on (θ,χ) and the dimensionality is reduced to two.

Even though the integrand in eqn. (8) does not depend on ϕ, the function $F(\theta,\chi)$ depends parametrically on the associated, 'space-fixed' projection quantum number m because of the form of the rotational basis functions $|J,k,m\rangle$.[56] The rotation–vibration energies are independent of m in the absence of external fields, but the corresponding eigenfunctions depend on this quantum number. We must therefore choose an m value for the wavefunctions that we analyze. We have found it useful to choose $m = J$. In an $m = J$ state, the molecule is aligned with the angular momentum oriented along the Z axis to the highest extent allowed by quantum mechanics. Consequently, in classical terms, the Z axis is the axis of rotation. The Euler angles θ,χ define the orientation of the molecule-fixed axis system xyz relative to the space fixed axis system XYZ.[41] When we plot the probability distribution of these Euler angles, we determine how the molecule prefers to align itself relative to the axis of rotation.

In Fig. 4, we show the rotational probability distributions obtained for the top-cluster wavefunctions $\psi_1^{A_1}$ and $\psi_6^{A_2}$ at $J = 40$. The function $F(\theta,\chi)$ is mapped onto a (Bloch) sphere of arbitrary radius. In the displays, we also indicate the equilibrium structure of the molecule and the molecule-fixed axis system xyz. On the surface of the sphere, we observe 'islands' with a higher probability density than the surrounding 'ocean', but these islands do not define a localization axis in the sense explained above. This is because the wavefunctions $\psi_1^{A_1}$ and $\psi_2^{A_2}$ have defined symmetries in $C_{3v}(M)$; they are linear combinations of the primitive cluster states $|1\ PCS\rangle$, $|2\ PCS\rangle$, $|3\ PCS\rangle$, $|4\ PCS\rangle$, $|5\ PCS\rangle$, and $|6\ PCS\rangle$ (Section III). In order to visualize the localization of the cluster states we must 'prepare' a primitive cluster state $|j\ PCS\rangle$ in terms of the symmetrized functions ψ_i^Γ, $i = 1, 2, \ldots, 6$. Towards this end we follow the approach of refs. 13 and 25: We neglect the small energy splittings between the six cluster states and consider them to be exactly degenerate. Under these circumstances, any linear combination of the six degenerate eigenfunctions ψ_i^Γ is also an eigenfunction of the rotation–vibration Hamiltonian. Using the standard projection operator methods discussed in Section 6.3 of ref. 42 we derive symmetrized linear combinations of the primitive cluster states $|j\ PCS\rangle$, $j = 1, 2, \ldots, 6$. For example, it is straightforward to show that the normalized linear combination

$$\frac{1}{\sqrt{6}}(|1\,PCS\rangle + |2\,PCS\rangle + |3\,PCS\rangle + |4\,PCS\rangle + |5\,PCS\rangle + |6\,PCS\rangle) \qquad (9)$$

has A_1 symmetry in $C_{3v}(M)$ and we identify it with the function $\psi_1^{A_1}$. Five further symmetrized linear combinations of the $|j\ PCS\rangle$ can be identified with ψ_2^E, ψ_3^E, ψ_4^E, ψ_5^E, and ψ_6^E, respectively. We have now expressed the ψ_i^Γ as linear combinations of the $|j\ PCS\rangle$, and by inverting this linear transformation we

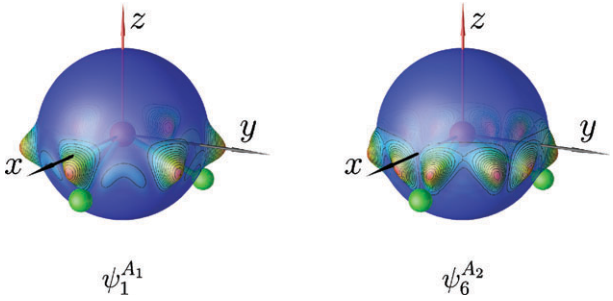

Fig. 4 Probability density functions $F(\theta,\chi)$ of the top-cluster wavefunctions $\psi_1^{A_1}$ and $\psi_6^{A_2}$ at $J = 40$, mapped onto a sphere of arbitrary radius. The molecule is given in its equilibrium configuration and the molecule-fixed axis system xyz is indicated.

express the $|j\ \mathrm{PCS}\rangle$ in terms of the ψ_i^Γ:

$$|j\ \mathrm{PCS}\rangle = \sum_{i,\Gamma} C_{i,\Gamma}^{(j)} \psi_i^\Gamma,\ j = 1, 2, ..., 6 \qquad (10)$$

where the $C_{i,\Gamma}^{(j)}$ are expansion coefficients. We do not give the details of the transformations here; the technique is discussed in considerable detail for XH_2 molecules in Section 4 of ref. 13.

A. Determination of the localization axes

The primitive cluster states $|j\ \mathrm{PCS}\rangle$ computed for the top clusters of XH_2 molecules were interpreted in terms of localization axes (see refs. 7 and 13, and the references therein). By rotating the $|j\ \mathrm{PCS}\rangle$ in space, an axis was identified onto which the projection of the angular momentum was $-J\hbar$ or $+J\hbar$; this is the localization axis (which can be thought of as the classical axis of rotation). It was found that the localization axis essentially coincides with one of the bonds in the XH_2 molecule. By necessity, this axis lies in the molecular plane and it can be located by rotating the $|j\ \mathrm{PCS}\rangle$ functions about an axis perpendicular to this plane. That is, for the XH_2 molecule only one rotation angle must be determined in order that the localization axis can be identified.

For the XH_3 molecules considered here, it is more complicated to determine the localization axes. The orientation of the localization axis A relative to the molecule-fixed axis system (see ref. 41) is given by two standard spherical coordinates θ_A, ϕ_A (the polar and azimuthal angles). For each primitive cluster state $|j\ \mathrm{PCS}\rangle$ we must generate the value of the projection of the angular momentum onto direction A, and vary θ_A, ϕ_A until this projection attains the value $-J\hbar$ or $+J\hbar$.

When we denote the unit vectors along the molecule-fixed xyz axes as $\mathbf{e}_x$, $\mathbf{e}_y$, and $\mathbf{e}_z$, respectively, a unit vector $\mathbf{e}_A$ along A is given by

$$\mathbf{e}_A = \sum_{\alpha=x,y,z} R_\alpha \mathbf{e}_\alpha, \qquad (11)$$

where

$$(R_x, R_y, R_z) = (\sin\theta_A \cos\phi_A,\ \sin\theta_A \sin\phi_A,\ \cos\theta_A). \qquad (12)$$

The projection of the angular momentum on axis A is represented by the operator

$$\mathbf{e}_A \cdot \boldsymbol{J} = R_x J_x + R_y J_y + R_z J_z. \qquad (13)$$

For a primitive cluster state $|j\ \mathrm{PCS}\rangle$, the projection of the angular momentum on the A axis is

$$J_A(\theta_A, \phi_A) = \langle j\ \mathrm{PCS}|\mathbf{e}_A \cdot \boldsymbol{J}|j\ \mathrm{PCS}\rangle = \sum_{i'',\Gamma''} \sum_{i',\Gamma''} \left(C_{i'',\Gamma''}^{(j)}\right)^* C_{i',\Gamma'}^{(j)} \sum_{\alpha=x,y,x} R_\alpha \langle \psi_{i''}^{\Gamma''} | J_\alpha | \psi_{i'}^{\Gamma'} \rangle. \qquad (14)$$

where we have used eqns. (10) and (13). We use the Newton–Raphson algorithm (see, for example, ref. 57) to maximize $J_A(\theta_A, \Phi_A)$ numerically for the top cluster wavefunctions at different J values. For each top cluster we obtain six equivalent localization axes connected by the symmetry operations in $C_{3v}(M)$. In terms of one polar angle value $\theta_A^{(0)}$ the six solutions are expressed as $(\theta_A, \phi_A) = (\theta_A^{(0)}, 0)$, $(\pi - \theta_A^{(0)}, \pi)$, $(\theta_A^{(0)}, 2\pi/3)$, $(\pi - \theta_A^{(0)}, 5\pi/3)$, $(\theta_A^{(0)}, 4\pi/3)$ and $(\pi - \theta_A^{(0)}, 7\pi/3)$. The values obtained for the polar angle $\theta_A^{(0)}$ for different values of J are given as squares in Fig. 5. At $J = 50$, the polar angle (which is the angle between the z axis and the A axis) is about 104°. Since the projection of $\boldsymbol{J}$ on the A axis is close to 50 $\hbar$, the absolute value of the projection on the z axis is approximately 50 $\hbar$ $|\cos 104°| \approx 12\ \hbar$. This explains why the wavefunctions in eqn. (7) have their maximum contributions from basis functions with K around 12.

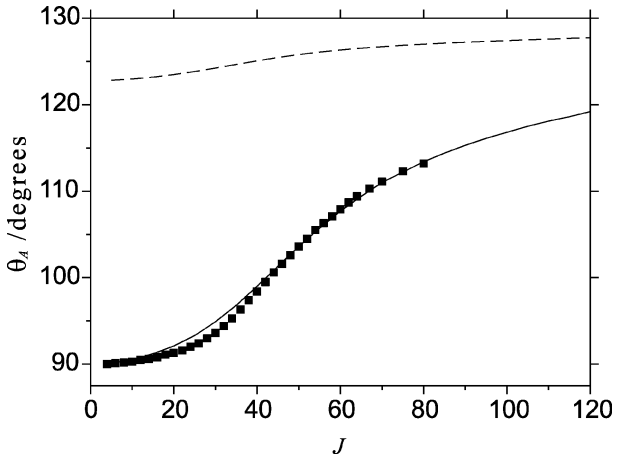

Fig. 5 Polar angles $\theta_A^{(0)}$ obtained by maximizing the function $J_A(\theta_A, \phi_A)$, eqn. (14), for different values of J (filled squares). The function $\theta(J)$ (solid curve) and the angle between the z axis and the P–H_1 bond (dashed curve) are obtained from semi-classical analysis (see text).

For low J values, the localization axes are perpendicular to the z axis; they lie along the axes with the smallest moments of inertia. For high J the localization axes tend towards the directions of the P–H bonds. The variation of the localization axes with J is rather smooth; there are none of the 'bifurcation' effects found in XH_2 molecules.[6] Fig. 5 shows that the cluster formation mechanism in PH_3 is different from that in XH_2 molecules, where the clusters form after a sudden change in the stability of the rotational axes. For PH_3, even the excitation to low-lying rotational states causes a change of the rotational axis. However, at the highest rotational excitation considered here, at $J = 80$, the localization axes do not coincide with the P–H bonds to the same extent as the localization axes for XH_2 molecules coincide with the X–H bonds already at $J < 40$. We illustrate this point by including as a dashed curve in Fig. 5 the angle between the z axis and the P–H_1 bond, obtained as a function of J from the semi-classical analysis described in Section V below. For the axis of rotation to coincide with the P–H_1 bond, this angle should be approximately equal to $\theta_A^{(0)}$, but this is not the case even at very high J, where we can compare with the semi-classical results for θ, given as a solid curve in Fig. 5. One reason that the rotation axis does not coincide with a bond is that the P nucleus simply is not heavy enough compared to the proton, and this moves the center of mass of PH_3 significantly away from the position of the P nucleus. Another reason is that in a situation where the localization axis coincides with, for example, the P–H_1 bond, the two bond angles $\alpha_3 = \angle(H_1PH_2)$ and $\alpha_2 = \angle(H_1PH_3)$ must become close to 90°, and a huge rotational excitation is required to achieve this. We show in Section V that the molecule dissociates by breaking of the P–H_2 and P–H_3 bonds before this limit is reached.

In Fig. 6 we show the probability density functions $F(\theta,\chi)$ for the primitive cluster function $|1\ \mathrm{PCS}\rangle$ at $J = 20$, 40, 60 and 80. In these distributions, we recognize that the localization axes A lie in the P–H_1–z plane and make up a rather well-defined polar angle θ with the z axis. In contrast to the functions visualized in Fig. 4, the primitive-cluster-state representation provides a very clear picture of the rotational localization. At low J a rotation axis approximately perpendicular to the z axis has maximum probability but there is no preferred azimuthal angle—the azimuthal distribution is broad. At $J = 80$ there is a distinct maximum at $\theta \approx 113°$. In the cluster states shown in Fig. 6, (anti-clockwise) rotation takes place about an axis near the P–H_1 bond, corresponding to $\chi \approx 0$. The other five primitive cluster states at a given J value, $|j\ \mathrm{PCS}\rangle$, $j = 2, 3, \ldots, 6$, produce $F(\theta,\chi)$-displays equivalent to those in Fig. 6. In Fig. 7 we present 1D probability distributions $f(\theta)$, calculated by

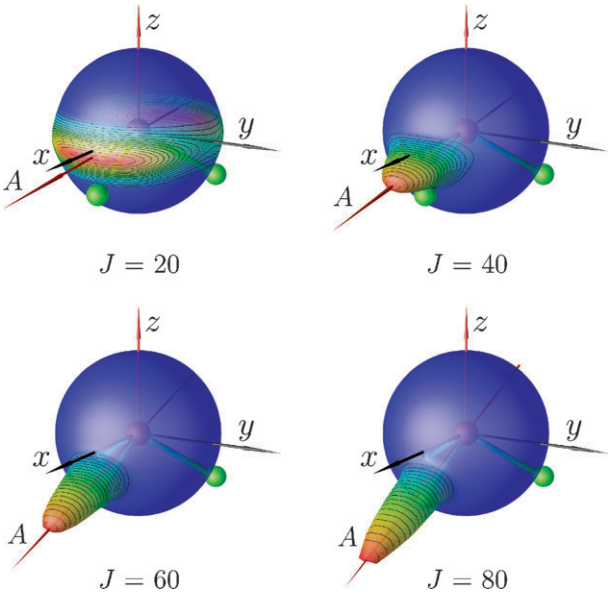

Fig. 6 Probability density functions $F(\theta,\chi)$ for the primitive cluster function $|1\ \mathrm{PCS}\rangle$ with $J = m = 20$, 40, 60 and 80. Even though $|1\ \mathrm{PCS}\rangle$ for $J = 20$ is not a true primitive cluster function (the corresponding energy levels are far from being degenerate), it is shown for comparison with the higher-J PCS functions.

further averaging $F(\theta,\chi)$ over the angle χ. Figs. 6 and 7 show that the probability distributions for $J = 20$, 40, 60 and 80 are localized about axes with $\theta = 94$, 98, 108 and 113°, respectively (for $\chi \approx 0$). This is in very good agreement with the θ_A values obtained by maximizing $J_A(\theta_A, \phi_A)$ (see Fig. 5).

We can now justify the choice of $m = J$ made for the visualization of the probability density functions $F(\theta,\chi)$. In Fig. 8 we show $F(\theta,\chi)$ functions obtained with $m = 0$ and 40, respectively, for the $J = 40$ top-cluster function $|1\ \mathrm{PCS}\rangle$. The display for $m = 40$ is identical to the $J = 40$ display in Fig. 6, but here we show it from a different perspective. When $m = 0$ in eqn. (6), all we know is that the angular momentum is approximately perpendicular to the Z axis, and this produces the $m = 0$ distribution in Fig. 8. This distribution does not give rise to alignment that we can use to identify the classical axis of rotation. Such alignment is obtained for the $m = 40$ distribution in the figure.

B. Expectation value analysis

In highly excited rotational states, the molecule deforms due to centrifugal forces. We now investigate the deformation in the

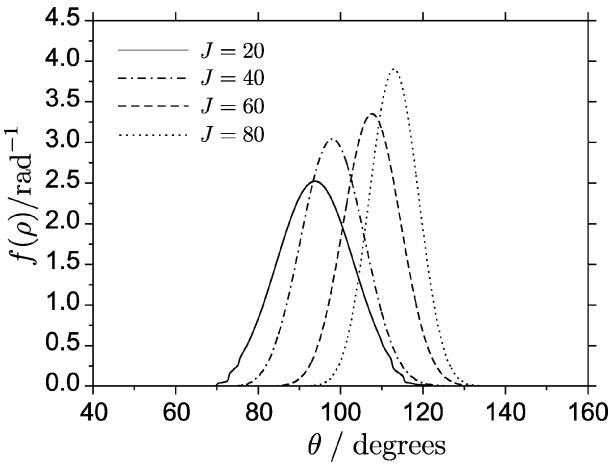

Fig. 7 1D probability distributions $f(\theta)$ for the primitive cluster function $|1\ \mathrm{PCS}\rangle$ with $J = m = 20$, 40, 60 and 80.

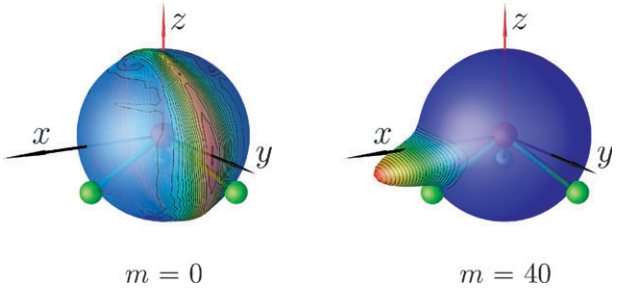

Fig. 8 Probability density functions $F(\theta,\chi)$ for the $|1\ \mathrm{PCS}\rangle$ top-cluster states with $(J,m) = (40,0)$ and (40,40), respectively.

cluster states by calculating expectation values of the vibrational coordinates p, ξ_λ^l (see Section II):

$$\bar{\rho} = \langle 1\ \mathrm{PCS}|\ \rho\ |1\ \mathrm{PCS}\rangle \tag{15}$$

and

$$\bar{\xi}_\lambda^l = \langle 1\ \mathrm{PCS}|\ \xi_\lambda^l\ |1\ \mathrm{PCS}\rangle. \tag{16}$$

The expectation values are calculated for the primitive cluster state $|1\ \mathrm{PCS}\rangle$, which corresponds to an axis of rotation localized near the P–H_1 bond. As we mentioned above, at low J, this state describes rotation about the axis with the smallest moment of inertia, which is perpendicular to the z axis (*i.e.*, the C_3 symmetry axis for the PH_3 molecule at equilibrium).

Although the six coordinate values $\bar{\rho}$, $\bar{\xi}_\lambda^l$ ($\lambda = 1, 2, 3, 4, 5$) fully determine the averaged geometry in the $|1\ \mathrm{PCS}\rangle$ state, it is clearly more illustrative to obtain the geometry in terms of the usual, geometrically defined bond lengths and bond angles. For this reason we define expectation values of bond lengths $\bar{r}_i$ and bond angles $\bar{\alpha}_i$ by means of the coordinate transformation established in ref. 41:

$$\bar{r}_i = r_i(\bar{\rho},\bar{\xi}_\lambda^l) \tag{17}$$

$$\bar{\alpha}_i = \alpha_i(\bar{\rho},\bar{\xi}_\lambda^l) \tag{18}$$

The calculated expectation values $\bar{r}_i$ and $\bar{\alpha}_i$ are given in Table 1 and plotted as squares in Figs. 9 and 10. For the bond lengths we plot the deviations of $\bar{r}_1$ and $\bar{r}_2 = \bar{r}_3$ from $r_0 = 1.424$ Å, the common expectation value of the three bond lengths in the rotation–vibration ground state (*i.e.*, for $J = 0$). For the bond angles we show the differences $\bar{\alpha}_1 - \bar{\alpha}_0$ and $\bar{\alpha}_2 - \bar{\alpha}_0$, where $\alpha_0 = 93.3°$ is the common expectation value for the three bond angles in the rotation–vibration ground state.

High rotational excitation causes dynamical symmetry breaking:[6] in the cluster states, the PH_3 molecule no longer has C_{3v} geometrical symmetry. In the $|1\ \mathrm{PCS}\rangle$ state, centrifugal forces stretch the two bonds P–H_2 and P–H_3 equally. The P–H_1 bond is also lengthened, but only slightly. All three bond angles $\bar{\alpha}_i$ are reduced by the rotational excitation, but the two angles $\alpha_2 = \angle(H_1PH_3)$ and $\alpha_3 = \angle(H_1PH_2)$, that involve the P–$H_1$ bond, remain equal as J increases and they are smaller than the

Table 1 Expectation values $\bar{r}_1$, $\bar{r}_2 = \bar{r}_3$, $\bar{\alpha}_1$ and $\bar{\alpha}_2 = \bar{\alpha}_3$ calculated at various values of J for the rotation–vibration state $|1\ \mathrm{PCS}\rangle$

J	$\bar{r}_1$/Å	$\bar{r}_1 = \bar{r}_3$/Å	$\bar{\alpha}_1$/°	$\bar{\alpha}_2 = \bar{\alpha}_3$/°
4	1.425	1.425	93.3	93.3
10	1.426	1.426	93.3	93.1
20	1.428	1.432	93.4	92.3
30	1.431	1.441	93.5	91.2
40	1.432	1.454	93.6	89.9
50	1.432	1.471	93.4	88.8
60	1.432	1.492	92.9	87.9
70	1.432	1.516	92.4	87.2
80	1.433	1.538	91.6	86.6

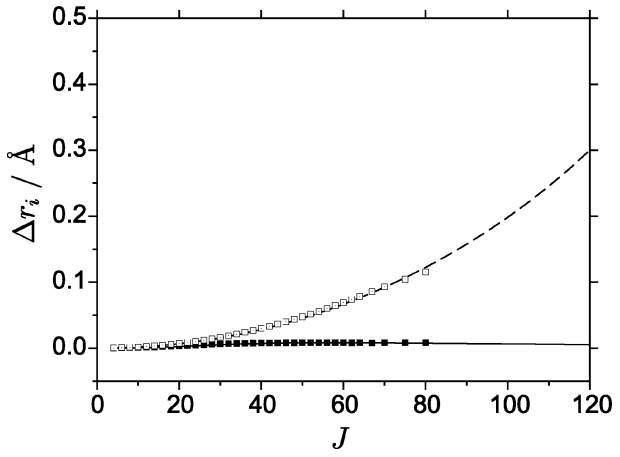

Fig. 9 The deviations of the $|1\ \mathrm{PCS}\rangle$-expectation values $\bar{r}_1$ (filled squares) and $\bar{r}_2 = \bar{r}_3$ (open squares) from the ground state value r_0 (see the text), and the deviations of the semi-classical stationary values of r_1 (solid curve) and r_2 (dashed curve) from the *ab initio* equilibrium bond length $r_e = 1.411$ Å.[48]

angle $\alpha_1 = \angle(H_2PH_3)$. The average structure has C_s geometrical symmetry with a reflection symmetry plane containing the H_1 and P nuclei while bisecting the bond angle α_1. The higher the J value, the higher is the degree of the structural distortion. At $J = 80$, $\bar{r}_1$ differs about 7% from $\bar{r}_2 = \bar{r}_3$.

V. Semi-classical analysis

As already mentioned, highly excited rotational states are accurately described by semi-classical models. Because semi-classical representation can provide additional insight into the nature of the rotational motion, we employ also models based on the rotational energy surface (RES)[21] here. The rotational motion of the system can be understood from the analysis of the stationary points on the RES. If the RES has N symmetrically equivalent stationary points, there will be N-fold degenerate energy clusters and, according to the analysis by Harter and Patterson,[21] the cluster states correspond to the set of the N smallest possible, classically allowed trajectories of $\boldsymbol{J}$ around the N stationary points.

The equations of motion for the rovibrational Hamiltonian H_{rv} are given by

$$\dot{q}_n = \partial H_{rv}/\partial p_n, \tag{19}$$

$$\dot{p}_n = -\partial H_{rv}/\partial q_n, \tag{20}$$

$$\dot{J}_\alpha = \{J_\alpha, H_{rv}\} \tag{21}$$

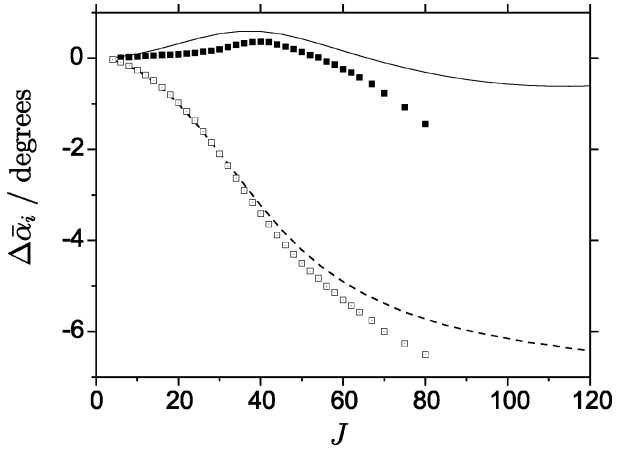

Fig. 10 The deviations of the $|1\ \mathrm{PCS}\rangle$-state expectation values $\bar{\alpha}_1$ (filled squares) and $\bar{\alpha}_2 = \bar{\alpha}_3$ (open squares) from the ground state value α_0 (see the text), and the deviations of the semi-classical stationary values of α_1 (solid curve) and α_2 (dashed curve) from the *ab initio* equilibrium bond angle $\alpha_e = 93.46°$.[48]

where, for a general variable x, $\dot{x} = \mathrm{d}x/\mathrm{d}t$ with t as time. In eqns. (19)–(21), the q_n represent the six generalized coordinates r_1, r_2, r_3, α_1, α_2, α_3, and $p_n = \partial T/\partial\dot{q}_n$ (where T is the classical kinetic energy) are the generalized momenta conjugate to q_n. J_α ($\alpha = x, y, z$) is the α-coordinate of the angular momentum $\boldsymbol{J}$ in the xyz axis system, and $\{A, B\}$ is a Poisson bracket. In eqns. (19)–(21), H_{rv} is the classical analogue of the quantum-mechanical rovibrational Hamiltonian employed in the variational calculations, *i.e.*, we use the same kinetic energy factor $G_{\alpha\beta}$, pseudo-potential U, and potential energy V. Owing to the large $J(J+1)$ factor in the kinetic energy part of H_{rv} and to the large displacements of the bond lengths (see Fig. 9) expected for $J > 80$, we expand $G_{\alpha\beta}$, U, and V through 6th order to ensure convergence in the semi-classical calculations. Solutions of eqns. (19)–(21) with the left hand sides set equal to zero gives stationary classical trajectories (or relative equilibria[58]). For XH_3 molecules with a high inversion barrier, such as PH_3, there are in total 14 stationary solutions near equilibrium.[58] The corresponding trajectories have the following symmetry elements: Two threefold axes, three reflection planes, and six twofold axes that lie in the planes containing one X–H bond and the centre of mass. The expectation value analysis has demonstrated that rotational excitation significantly distorts the molecule. Consequently, in our search for the stationary solutions of eqns. (19)–(21), we allow large displacements from equilibrium. Employing the Newton–Raphson algorithm, we have scanned for stable stationary solutions for $J < 140$. For all values of $J < 120$ we find eight stable solutions: Two of the solutions minimize the energy and correspond to rotation about the z axis (the axis with the largest moment of inertia). The other six solutions maximize the rotational energy and correspond to rotations about axes that lie in the planes containing a P–H bond and the z axis. These latter six solutions are grouped in three pairs. For each pair, the axes of rotation for the two pair solutions form polar angles of $\theta(J)$ and $\pi - \theta(J)$, respectively, with the z axis, and have a common value of the azimuthal angle. The function $\theta(J)$ is common for all three solution pairs. These solution pairs correspond to azimuthal angles for the axes of rotation of 0, $2\pi/3$, and $4\pi/3$, respectively. The six stable semi-classical solutions with maximum energy correspond to the six-fold energy clusters discussed above. For $J > 120$ the search for stationary points becomes unstable because the molecule is now close to dissociation.

To visualize the semi-classical description of the rotation we plot rotational energy surfaces obtained by standard methods.[21] The xyz components of the quantum-mechanical angular momentum operator $\boldsymbol{J}$ are replaced by their classical analogues:

$$J_x = \sqrt{J(J+1)}\sin\theta_J\cos\phi_J \tag{22}$$

$$J_y = \sqrt{J(J+1)}\sin\theta_J\sin\phi_J \tag{23}$$

$$J_z = \sqrt{J(J+1)}\cos\theta_J \tag{24}$$

The rotational energy $E_J(\theta_J, \Phi_J)$ is then given by

$$E_J(\theta_J, \Phi_J) = H_{rv}(q_n = q_n^s, p_n = p_n^s, J, \theta_J, \phi_J), \tag{25}$$

where the classical Hamiltonian function H_{rv} is calculated at the stationary geometries (q_n^s, p_n^s) at different polar and azimuthal angles (θ_J, Φ_J) that define the direction of the angular momentum in the xyz axis system. A rotational energy surface is a radial plot of $E_J(\theta_J, \Phi_J) - E_J(\theta_{min}, \Phi_{min})$, where $E_J(\theta_{min}, \Phi_{min})$ is the minimum value of $E_J(\theta_J, \Phi_J)$, given in arbitrary units. In Fig. 11 we present such rotational energy surfaces obtained for PH_3 at $J = 20$, 40, 60, 80, 100 and 120. The figure shows that as J increases from 20 to 40, the rotational energy surface develops six equivalent maxima which become more pronounced as J increases further. The low-J rotational

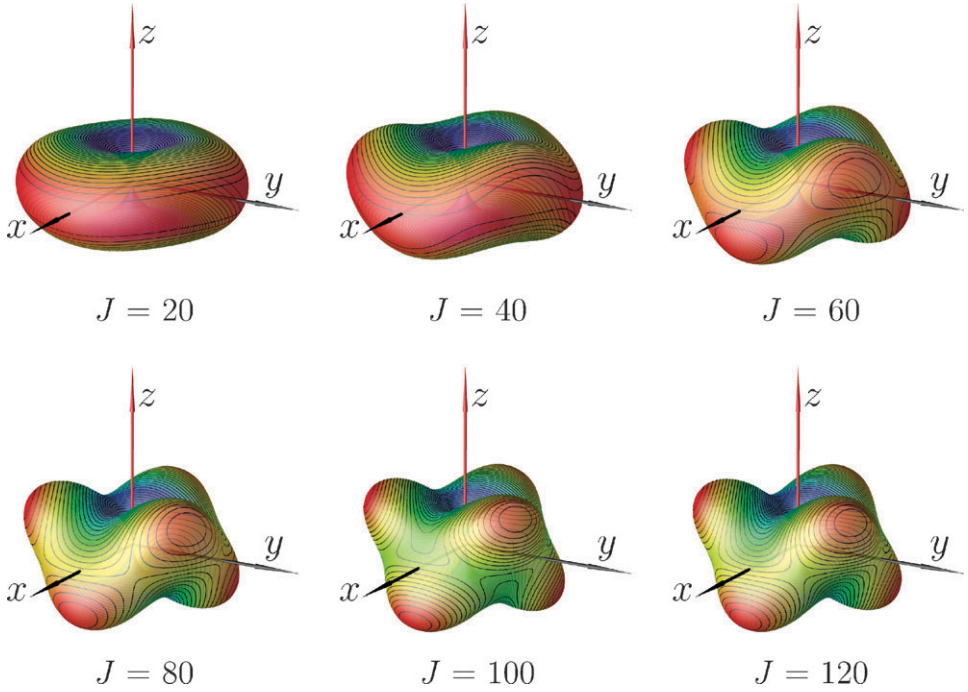

Fig. 11 Rotational energy surfaces for PH_3 calculated for $J = 20$, 40, 60, 80, 100 and 120.

surfaces have a doughnut-like torus structure[24] similar to the rotational energy surface for a rigid PH_3 molecule:

$$E_J^{(\mathrm{rigid})}(\theta_J,\phi_J) - E_J^{(\mathrm{rigid})}(\theta_{\min},\phi_{\min}) = |B_e - C_e|\, J(J+1) \times \sin^2\theta_J; \qquad (26)$$

this expression is straightforwardly obtained from the results in Section 11.2.1 of ref. 42. The six-fold top clusters in the vibrational ground state of PH_3 are described by the six equivalent maxima on the high-J rotational energy surfaces. In the Harter–Patterson theory mentioned above,[21] the six cluster states correspond to six symmetrically equivalent, classically allowed trajectories of the classical angular momentum J on the rotational energy surface: each of these trajectories is a precession of J around one of the maxima.

In the semi-classical treatment we obtain the stationary values of r_i and α_i as functions of J. These values are included in Figs. 9 and 10 for comparison with the corresponding quantum-mechanical results. Also in the semi-classical picture the rotational excitation produces dynamical breaking of the C_{3v} geometrical symmetry.

The semi-classical results for the bond lengths and bond angles are in very good agreement with the quantum-mechanical values. It is also illustrative to examine the difference $\alpha_1 - \alpha_2$, which is a measure of the geometrical distortion. We plot these differences in Fig. 12, where we also present (as filled squares) the corresponding quantum-mechanical expectation values $\bar{\alpha}_1 - \bar{\alpha}_2$. For $J > 70$, $\bar{\alpha}_1 - \bar{\alpha}_2$ deviates significantly from the semi-classical value. This is presumably because the vibrational basis set used for the quantum mechanical calculation is not adequate at these J values. We consider the semi-classical results to be more reliable in this J range.

The semi-classical polar angle $\theta(J)$ is plotted as a solid curve in Fig. 5 where it is compared to the quantum-mechanical values of $\theta_A^{(0)}$ obtained by maximizing the function $J_A(\theta_A,\phi_A)$ in eqn. (14). The agreement is very good for all J values considered here. This suggests that the semi-classical description of the rotational motion is reliable also at very high J where quantum mechanical calculations are currently not feasible. We can use the semi-classical $\theta(J)$-curve in Fig. 5 to estimate that the angle between the P–H_1 bond and the axis of rotation is reduced to 8.6° at $J = 120$. However, to reach this point one would need to excite the molecule by 6.5 eV of rotational

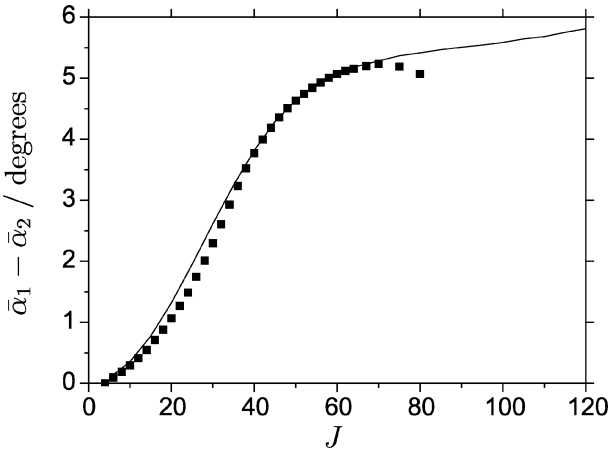

Fig. 12 The $|1\,\mathrm{PCS}\rangle$ expectation values $\bar{\alpha}_1 - \bar{\alpha}_2$ (filled squares), compared to the stationary values of $\alpha_1 - \alpha_2$ determined from semi-classical theory (solid curve).

energy, which exceeds the bond dissociation energy of $D_0 \approx 3.58$ eV (82.46 ± 0.46 kcal mol^{-1} [59]). Thus, we cannot in practice excite the molecule to states with $J = 120$. The potential energy surface used here has a dissociation energy D_e of around 8.4 eV for a dissociation process where the two bonds are stretched as shown in Fig. 9 while the bond angles vary as shown in Fig. 10.

VI. Discussion and conclusion

We have shown that 'deformation' effects, in the form of centrifugal distortion, are playing an important role in the high-energy rotational dynamics of PH_3. As pointed out previously[6] for XH_2 molecules: "The physical reasons for... [the formation of rotation–vibration energy clusters]... lie in the molecular symmetry and in the anisotropic centrifugal forces". The analysis shows that centrifugal forces destroy the C_{3v} equilibrium structure of PH_3 and cause qualitative changes in the spectral pattern.

The energy cluster formation in PH_3 is analogous to that in XH_2 molecules in the sense that the term value diagram in

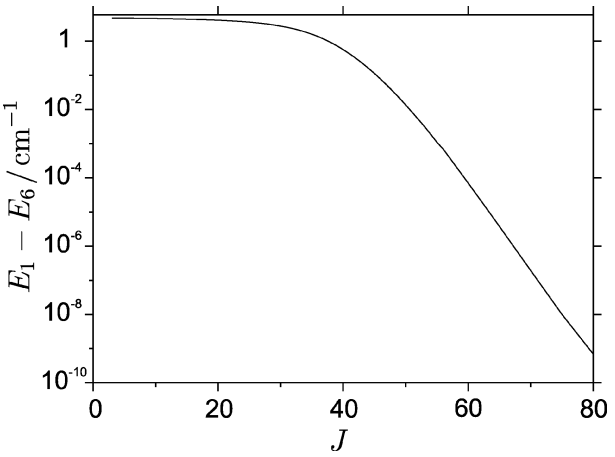

Fig. 13 The cluster spread (see text) for the top cluster in the vibrational ground state of PH_3 plotted as a function of J.

Fig. 2 is similar to the corresponding diagrams drawn for XH_2 molecules (see, for example, refs. 25, 26, 31, 49 and 50). Nevertheless, the dynamical processes causing the cluster formation are qualitatively different for XH_2 and XH_3 molecules. In the XH_2 case, bifurcation effects are responsible for forming the cluster pattern: As J increases, the axes with the smallest moments of inertia lose their stability and the molecule starts rotating about new stable axes that approach the X–H bonds at high J values. For XH_3 molecules, no such sudden 'axis switching' occurs. There is no bifurcation at a critical J_c value.[6] However, by analyzing the rotational dynamics of PH_3 in the vibrational ground state, we find the following characteristic J values: (i) Already at low J values, there is significant molecular deformation due to centrifugal forces. (ii) At $J = 12$–13 in the term value diagram Fig. 2, the $|k| = 3$ levels split apart and the highest component [with symmetry A_2 (A_1) for J even (odd)] starts approaching the other levels in the top cluster, whereas the lowest $|k| = 3$ component [with symmetry A_1 (A_2) for J even (odd)] starts approaching the other levels in the second cluster from the top. (iii) From $J = 32$–34 onwards we see in Fig. 2 a rapid decrease in the energy splitting between the highest level in each J stack [$k = 0$; symmetry A_1 (A_2) for J even (odd)] and the level below it ($k = 1$; symmetry E), and in the splitting between the highest $|k| = 3$ component and the level above it ($k = 2$; symmetry E). (iv) At low J, the P–H_1 bond closest to the rotational axis A stretches slightly with increasing J, but at $J \approx 40$ it stops increasing. The 'opposite' bond angle α_i, which involves the two other bonds, initially increases with J but attains a maximum value and starts decreasing at $J \approx 40$. (v) According to the semi-classical RES analysis, centrifugal forces cause the molecule to dissociate at $J > 120$.

Fig. 13 is a logarithmic-scale plot of the 'cluster spread' $E_1 - E_6$, *i.e.*, the difference between the highest and lowest energy in the top cluster obtained from the quantum-mechanical calculation, as a function of J. For high J, the cluster spread decreases exponentially with J and the figure obviously suggests that $E_1 - E_6 \to 0$ for $J \to \infty$.

The cluster spread for the four-fold top clusters in the vibrational ground state of an XH_2 molecule (see ref. 7 and the references therein) attains its maximum value at the critical J value J_c: It increases with J for $J < J_c$ and decreases rapidly for $J > J_c$. This behaviour is a result of the 'bifurcation' process mentioned above. The formation of the six-fold top clusters in PH_3 is a more gradual process, and so the cluster spread in Fig. 13 decreases monotonically with J. However, the curve in Fig. 13 indicates that between $J = 30$ and 40, a critical change in the dynamics takes place for PH_3. For $J > 40$, the rate of decrease of $E_1 - E_6$ with J is vastly accelerated relative to the situation for $J < 30$. This behaviour is undoubtedly related to the emergence of the six equivalent maxima on the rotational energy surfaces in Fig. 11. Based on Fig. 13, we can say that the critical J value $J_c \approx 35$ for the vibrational ground state of PH_3.

The smoothness of the curve in Fig. 13 is an indication that our computed energies are numerically very accurate. It seems unlikely that numerical errors, such as round-off effects, would influence all cluster energies at a given J in the same way since these energies are eigenvalues of different matrix blocks with different dimensions. If numerical errors were significant, they should cause the cluster spreads to fluctuate in a seemingly random manner as J changes. However, as seen in Fig. 13, no such effects are detectable.

In addition to the top cluster states, we have examined the states of lowest energy in each J stack for PH_3. In these states, the molecule has C_{3v} geometrical symmetry and rotates about the C_3 axis which, as the c axis, has the highest moment of inertia, so rotation about it produces the lowest possible rotational energy. Centrifugal forces cause the bond lengths and bond angles to increase and one could imagine that, at sufficiently high rotational excitation, the molecule would acquire a planar structure with D_{3h} geometrical symmetry. Because of the high potential-energy barrier to planarity, which must be overcome by the centrifugal forces, this requires an extreme excitation. At $J = 60$ the expectation value analysis predicts that the bond angles have increased by 5.9° relative to the average values for $J = 0$, so that their common value is 99.2°, still much smaller than the value of 120° for the planar structure with D_{3h} geometrical symmetry. At $J = 120$, the semi-classical value of the bond angle reaches 108°.

The fast rotation in the high-J states causes stretching of the molecular bonds and deformation of the bond angles. Since, in the quantum-mechanical model, centrifugal distortion is described by an admixture of excited vibrational basis states in the linear-combination expression [eqn. (6)] for the ground state wavefunction, the limited basis set [eqn. (2)] becomes critical. The contributions to the top cluster states from excited vibrational basis states increase as J increases. For example, at $J = 60$ the major contribution, of about 63%, to the wavefunction $\psi_1^{A_1}$ originates in the vibrational basis state $|v = 0\rangle$ that correlates with the vibrational ground state. Other significant contributions come from the primitive stretching basis functions with $v_1 + v_2 + v_3 = 1$ (21%), bending functions with $v_b = 1$ (8%), and inversion functions with $v_i = 1$ (0.2%). At $J = 80$ the primitive stretching basis functions with $v_1 + v_2 + v_3 = 1$ contribute 34%, almost as much as the 35% coming from $|v = 0\rangle$. The stretching basis states at highest energy, with $v_1 + v_2 + v_3 = 3$, have a 2% contribution, and so the basis set is probably not quite sufficient at $J = 80$.

We consider our variational approach with implemented wavefunction-analysis tools as a first step towards theoretical studies of laser-induced molecular rotational dynamics. We are interested in studying the laser alignment of molecules, including 3D alignment. Our approach is suitable for elucidating the dynamics of the XY_3 molecule after the laser field has been applied and needs only a minor extension to describe also the situation of the molecule in the laser field (see, for example, ref. 1).

Acknowledgements

The initial stages of this work were supported by the European Commission through contract no. HPRN-CT-2000-00022 'Spectroscopy of Highly Excited Rovibrational States'. We are grateful to S. Petrov for his interest and valuable comments. We thank O. N. Ulenikov for providing a copy of the QWanew program and P. R. Bunker for helpful discussions. The work of P. J. is supported in part by the Deutsche Forschungsgemeinschaft and the Fonds der chemischen Industrie.

References

1 H. Stapelfeldt and T. Seideman, *Rev. Mod. Phys.*, 2003, **75**, 543–557.
2 D. A. Baugh, D. Y. Kim, V. A. Cho, L. C. Pipes, J. C. Petteway and C. D. Fuglesang, *Chem. Phys. Lett.*, 1994, **219**, 207–213.
3 J. Karczmarek, J. Wright, P. Corkum and M. Ivanov, *Phys. Rev. Lett.*, 1999, **82**, 3420–3423.
4 D. M. Villeneuve, S. A. Aseyev, P. Dietrich, M. Spanner, M. Yu. Ivanov and P. B. Corkum, *Phys. Rev. Lett.*, 2000, **85**, 542–545.
5 B. I. Zhilinskii and I. M. Pavlichenkov, *Opt. Spectrosc. (USSR)*, 1988, **64**, 413–414.
6 I. N. Kozin and I. M. Pavlichenkov, *J. Chem. Phys.*, 1996, **104**, 4105–4113.
7 P. Jensen, G. Osmann and I. N. Kozin, in *Vibration-Rotational Spectroscopy and Molecular Dynamics*, ed. D. Papoušek, World Scientific, Singapore, 1997.
8 M. S. Child, *J. Phys. A*, 1998, **31**, 657–670.
9 M. S. Child, T. Weston and J. Tennyson, *Mol. Phys.*, 1999, **96**, 371–379.
10 I. N. Kozin and R. M. Roberts, *J. Chem. Phys.*, 2003, **118**, 10523–10533.
11 M. S. Child and L. Halonen, *Adv. Chem. Phys.*, 1984, **57**, 1–58.
12 L. Halonen and A. G. Robiette, *J. Chem. Phys.*, 1986, **84**, 6861–6871.
13 P. Jensen, *Mol. Phys.*, 2000, **98**, 1253–1285.
14 K. K. Lehmann, *J. Chem. Phys.*, 1991, **95**, 2361–2370.
15 A. J. Dorney and J. K. G. Watson, *J. Mol. Spectrosc.*, 1972, **42**, 135–148.
16 W. G. Harter, C. W. Patterson and F. J. da Paixao, *Rev. Mod. Phys.*, 1978, **50**, 37–83.
17 W. G. Harter, H. W. Galbraith and C. W. Patterson, *J. Chem. Phys.*, 1978, **69**, 4888–4895.
18 W. G. Harter, C. W. Patterson and H. W. Galbraith, *J. Chem. Phys.*, 1978, **69**, 4896–4907.
19 C. W. Patterson, H. W. Galbraith, B. J. Krohn and W. G. Harter, *J. Mol. Spectrosc.*, 1979, **77**, 457–473.
20 W. G. Harter and C. W. Patterson, *Phys. Rev. A*, 1979, **19**, 2277–2303.
21 W. G. Harter and C. W. Patterson, *J. Chem. Phys.*, 1984, **80**, 4241–4261.
22 C. W. Patterson, *J. Chem. Phys.*, 1985, **83**, 4618–4632.
23 W. G. Harter, *J. Chem. Phys.*, 1986, **85**, 5560–5574.
24 W. G. Harter, *Comp. Phys. Rep.*, 1988, **8**, 319–394.
25 P. Jensen and I. N. Kozin, *J. Mol. Spectrosc.*, 1993, **160**, 39–57.
26 I. N. Kozin and P. Jensen, *J. Mol. Spectrosc.*, 1993, **161**, 186–207.
27 J. Makarewicz and J. Pyka, *Mol. Phys.*, 1989, **68**, 107–127.
28 J. Makarewicz, *Mol. Phys.*, 1990, **69**, 903–921.
29 J. Pyka, *Mol. Phys.*, 1990, **70**, 547–561.
30 I. N. Kozin, S. Klee, P. Jensen, O. L. Polyanski and I. M. Pavlichenkov, *J. Mol. Spectrosc.*, 1993, **158**, 409–422.
31 P. C. Gómez and P. Jensen, *J. Mol. Spectrosc.*, 1997, **185**, 282–289.
32 S. Brodersen and B. I. Zhilinskii, *J. Mol. Spectrosc.*, 1995, **172**, 303–318.
33 D. A. Sadovskii, B. I. Zhilinskii, J. P. Champion and G. Pierre, *J. Chem. Phys.*, 1990, **92**, 1523–1537.
34 K. Fox, H. W. Galbraith, B. J. Krohn and J. D. Louck, *Phys. Rev. A*, 1977, **15**, 1363–1381.
35 S. M. Colwell, N. C. Handy and W. H. Miller, *J. Chem. Phys.*, 1978, **68**, 745–749.
36 P. Jensen and I. N. Kozin, *J. Mol. Spectrosc.*, 1994, **163**, 483–509.
37 I. N. Kozin, S. P. Belov, O. L. Polyanski and M. Yu. Tretyakov, *J. Mol. Spectrosc.*, 1992, **152**, 13–28.
38 I. N. Kozin, O. L. Polyanski, S. I. Pripolzin and V. L. Vaks, *J. Mol. Spectrosc.*, 1992, **156**, 504–506.
39 J. P. Aldridge, H. Filip, H. Flicker, R. F. Holland, R. S. McDowell, N. G. Nereson and K. Fox, *J. Mol. Spectrosc.*, 1975, **58**, 165–168.
40 H. Lin, W. Thiel, S. N. Yurchenko, M. Carvajal and P. Jensen, *J. Chem. Phys.*, 2002, **117**, 11265–11276.
41 S. N. Yurchenko, M. Carvajal, P. Jensen, H. Lin, J. Zheng and W. Thiel, *Mol. Phys.*, 2005, **103**, 359–378.
42 P. R. Bunker and P. Jensen, *Molecular Symmetry and Spectroscopy*, NRC Research Press, Ottawa, 2nd edn., 1998.
43 D. Papoušek, J. M. R. Stone and V. Špirko, *J. Mol. Spectrosc.*, 1973, **48**, 17–37.
44 P. Jensen, *Comput. Phys. Rep.*, 1983, **1**, 1–55.
45 J. W. Cooley, *Math. Comput.*, 1961, **15**, 363–374.
46 E. B. Wilson Jr., J. C. Decius and P. C. Cross, *Molecular Vibrations*, McGraw-Hill, New York, 1955.
47 S. N. Yurchenko, M. Carvajal, P. Jensen, F. Herregodts and T. R. Huet, *Chem. Phys.*, 2003, **290**, 59–67.
48 D. Wang, Q. Shi and Q.-S. Zhu, *J. Chem. Phys.*, 2000, **112**, 9624–9631.
49 P. Jensen, Yan Lee, G. Hirsch, R. J. Buenker, T. J. Lee and I. N. Kozin, *Chem. Phys.*, 1995, **190**, 179–189.
50 I. N. Kozin and P. Jensen, *J. Mol. Spectrosc.*, 1994, **163**, 483–509.
51 P. Jensen and P. R. Bunker, *J. Mol. Spectrosc.*, 1994, **164**, 315–317.
52 D. Papoušek and M. R. Aliev, *Molecular Vibrational-Rotational Spectra*, Elsevier, Amsterdam, 1982.
53 O. N. Ulenikov, G. A. Onopenko, N. E. Tyabaeva, S. Alanko, M. Koivusaari and R. Anttila, *J. Mol. Spectrosc.*, 1997, **186**, 293–313.
54 L. Fusina and G. Di Lonardo, *J. Mol. Struct.*, 2000, **517–518**, 67–78.
55 R. P. Feynman, *Statistical Mechanics*, Benjamin-Cummings, Reading, MA, 1972.
56 R. N. Zare, *Angular Momentum*, Wiley, NewYork, 1988.
57 J. M. Thijssen, *Computational Physics*, Cambridge University Press, Cambridge, 1999.
58 J. A. Montaldi and R. M. Roberts, *J. Nonlinear Sci.*, 1999, **9**, 53–88.
59 J. Berkowitz, L. A. Curtiss, S. T. Gibson, J. P. Greene, G. L. Hillhouse and J. A. Pople, *J. Chem. Phys.*, 1986, **84**, 375–384.

